

General relativistic simulations of magnetized binary neutron star mergers

Yuk Tung Liu,¹ Stuart L. Shapiro,^{1,*} Zachariah B. Etienne,¹ and Keisuke Taniguchi¹

¹*Department of Physics, University of Illinois at Urbana-Champaign, Urbana, IL 61801*

Binary neutron stars (NSNS) are expected to be among the leading sources of gravitational waves observable by ground-based laser interferometers and may be the progenitors of short-hard gamma ray bursts. We present a series of general relativistic NSNS coalescence simulations both for unmagnetized and magnetized stars. We adopt quasiequilibrium initial data for circular, irrotational binaries constructed in the conformal thin-sandwich (CTS) framework. We adopt the BSSN formulation for evolving the metric and a high-resolution shock-capturing scheme to handle the magnetohydrodynamics. Our simulations of unmagnetized binaries agree with the results of Shibata, Taniguchi and Uryū [1]. In cases in which the mergers result in a prompt collapse to a black hole, we are able to use puncture gauge conditions to extend the evolution and determine the mass of the material that forms a disk. We find that the disk mass is less than 2% of the total mass in all cases studied. We then add a small poloidal magnetic field to the initial configurations and study the subsequent evolution. For cases in which the remnant is a hypermassive neutron star, we see measurable differences in both the amplitude and phase of the gravitational waveforms following the merger. For cases in which the remnant is a black hole surrounded by a disk, the disk mass and the gravitational waveforms are about the same as the unmagnetized cases. Magnetic fields substantially affect the long-term, secular evolution of a hypermassive neutron star (driving ‘delayed collapse’) and an accretion disk around a nascent black hole.

PACS numbers: 04.25.D-, 04.25.dk, 04.30.-w

I. INTRODUCTION

There is great interest in studying the effects of magnetic fields in relativistic astrophysics. Magnetic fields are always present in astrophysical plasmas, which are usually highly conducting. Even if the initial magnetic field is small, it can be amplified via magnetic winding and other magnetic instabilities (see, e.g., [2, 3] for reviews). Neutron stars (NSs) have the strongest observed magnetic fields (up to $\sim 10^{15}$ G) among astrophysical objects [4]. The strong magnetic fields result from gravitational collapse, which amplifies the magnetic fields in the core of the progenitor, and from various dynamo processes after the collapse (see, e.g., [5] for a review). Strong magnetic fields in a NS may trigger observable events such as pulsar glitches and the emission of large bursts of gamma rays and X-rays as in a soft gamma-ray repeater. Magnetic fields in a binary neutron star (NSNS) system may also influence the dynamics of the remnant after the NSs merge.

Mergers of binary neutron stars (NSNSs) are expected to be among the leading sources of gravitational waves observable by ground-based laser interferometers. Observations of short-hard gamma-ray bursts (GRBs) suggest that a substantial fraction of them may be formed from mergers of NSNSs or mergers of neutron star-black hole binaries (BHNs). Many theoretical models of GRB engines consist of magnetized accretion disks around a spinning black hole [6, 7, 8]. General relativistic magne-

tohydrodynamics (GRMHD) is necessary to model such systems.

The first two GRMHD codes capable of evolving the GRMHD equations in *dynamical* spacetimes were developed by Duez et al. [9] (hereafter DLSS) and Shibata & Sekiguchi [10] (hereafter SS). These codes are based on the BSSN (Baumgarte-Shapiro-Shibata-Nakamura) scheme to integrate the Einstein field equations, a high-resolution shock-capturing (HRSC) scheme to integrate the MHD and induction equations, and a constrained transport scheme to enforce the “no-monopole” magnetic constraint. Subsequently, Giacomazzo & Rezzolla [11] and Anderson et al. [12] developed similar codes. Our code (DLSS) and the code of SS have been used to study magnetic fields in hypermassive neutron stars [13, 14, 15], magnetorotational collapse of massive stellar cores to neutron stars [16], and (unmagnetized) coalescing BHNs [17, 18, 19, 20]. We have also used our code to study the magnetorotational collapse of massive stellar cores to black holes [21] as well as coalescing BHBs [22], which are pure vacuum simulations. Shibata et al. have also performed simulations of (unmagnetized) coalescing NSNSs [1, 23, 24, 25, 26].

Recently, Anderson et al. have used their code to study the coalescence of both unmagnetized and magnetized NSNSs [27, 28]. In the unmagnetized cases, they find an initial configuration in [27] that leads to prompt collapse to a black hole following the merger. The total (baryon) rest mass of their initial configuration is $M_0 \approx 1.03M_0^{(\text{TOV})}$ [29], where $M_0^{(\text{TOV})}$ is the maximum rest mass of a nonrotating neutron star for the $n=1$ polytropic equation of state (EOS) adopted in their simulation. This result seems to contradict the earlier finding of Shibata, Taniguchi & Uryū [1] that prompt

*Also at Department of Astronomy and NCSA, University of Illinois at Urbana-Champaign, Urbana, IL 61801

black hole formation is possible for this EOS only if $M_0 \gtrsim 1.7M_0^{(\text{TOV})}$. We note, however, that the initial data used by Shibata et al. and Anderson et al. are different. Shibata et al. use quasiequilibrium initial data for binaries in nearly circular orbits constructed using the conformal thin-sandwich (CTS) method. In contrast, Anderson et al. set up the initial data by superposing boosted metrics of two spherical neutron stars. Anderson et al.'s initial data results in an orbital eccentricity of about 0.2 [27], whereas the eccentricities of the CTS initial data are $\lesssim 0.015$ according to a post-Newtonian analysis [30]. We point out that a quasi-circular orbit is more realistic because gravitational radiation would have circularized the orbit long before the binary separation reaches a few NS radii. Also, a NS in a quasiequilibrium circular orbit will be distorted by tidal effects.

Anderson et al. report in [28] that a NSNS with the same EOS and masses as in [27] but with different initial separation leads to a hypermassive neutron star after the merger. Later, the star undergoes ‘delayed collapse’ to a black hole due to gravitational radiation. This finding is also surprising. The total rest mass $M_0 \approx 1.03M_0^{(\text{TOV})}$ is smaller than the maximum mass of a uniformly rotating star (the supramassive limit), $M_0^{(\text{sup})} = 1.15M_0^{(\text{TOV})}$ [31]. Hence the remnant cannot be a hypermassive NS, i.e. a NS whose mass exceeds the supramassive limit. As a result, the star will be unstable to gravitational collapse only if a very large amount of angular momentum is removed. A priori, the expected outcome is that gravitational radiation removes only some of the angular momentum, the remnant acquires some differential rotation, and the star settles down to a stable, stationary, rotating configuration.

To better understand the coalescence of NSNSs and the role of magnetic fields, we perform a new series of simulations using our DLSS code. In this paper, we consider three models, using the same CTS initial data as in [1]. Specifically, we study the irrotational binary models M1414, M1616 and M1418 in [1]. In models M1414 and M1616, the NSs are of equal mass. In model M1418, the ratio of the rest masses of the two NSs are $q=0.855$.

We first repeat the calculations of Shibata, Taniguchi & Uryū [1] for unmagnetized NSNS mergers. Our results agree with those reported in [1]. Model M1414 results in a dynamically stable, differentially rotating hypermassive NS. For models M1616 and M1418, the mergers lead to prompt collapse to a black hole. The simulations in [1] are terminated soon after black hole formation because of grid stretching. We are able to follow the evolution using puncture gauge conditions (see, e.g. [32, 33]) until the system settles down to a quasi-equilibrium state. This allows us to estimate the disk mass around the black hole more accurately, and our results are again consistent with those estimated in [1]. We next consider the magnetized cases. We add a poloidal field with strength $B \sim 10^{16}\text{G}$ inside each NS of the three NSNS models and follow the evolution. While such interior field strength may be larger than the value expected for a typical NS, it

is comparable to the strength inferred for magnetars [34] and is high enough to demonstrate the dynamical effects of a magnetic field, if any. For model M1414, the merger again results in a differentially rotating, hypermassive neutron star. We see observable difference in the magnetized case after the merger as magnetic fields are amplified. For model M1616, the system collapses to a black hole after the merger as before, leaving negligible amount of material to form a disk. This result is unaffected by the presence of the magnetic field. For model M1418, about 1.5% of rest mass is left to form a disk for both magnetized and unmagnetized cases. Gravitational waveforms for models M1616 and M1418 show only a slight difference in amplitude during the entire simulations. This is because the remnants quickly collapse to a black hole after the merger and magnetic fields do not have enough time to amplify and alter the dynamics of the fluid substantially. This result is not surprising since the ratio of magnetic to gravitational potential energy is $E_M/|W| \sim 10^{-4}$ initially, and hence the magnetic fields are not expected to have an impact on the dynamics before they are amplified.

For models M1414 and M1418, magnetic fields are expected to affect the *long-term* secular evolution of the remnants. For the cases where the remnant is a hypermassive neutron star (M1414), magnetic fields are crucial for driving ‘delayed collapse’ of the star [13, 15], and the resulting remnant could be a central engine for a short-hard GRB [14]. The effect of a magnetic field may be diminished whenever the merged hypermassive remnants develop a bar [25, 26]. The bar leads to dissipation of angular momentum by gravitational radiation and may result in delayed collapse on a timescale faster than that of magnetic field amplification. However, a bar does not develop for model M1414. In general, the development of a bar depends on the NS EOS. For cases in which the remnant consists of a black hole surrounded by a disk (M1418), magnetic fields may produce turbulence in the disk via MHD instabilities and may generate ultra-relativistic jets [35, 36, 37, 38, 39, 40, 41]. In this paper, we are primarily interested in studying the effect of the magnetic field during the late inspiral, merging and the early post-merger phases, so we do not follow the long-term evolution of the remnants. We have previously studied the long-term secular evolution of magnetized hypermassive NSs in [13, 15] and the evolution of magnetized disks around rotating black holes in [42].

This paper is organized as follows. In Sec II, we briefly summarize the basic equations and their specific implementation in our GRMHD scheme. In Sec. III, we present the results of our simulations and compare them with those in [1]. We summarize our results in Sec. IV and comment on future directions.

II. FORMULATION

A. Basic equations and numerical methods

The formulation and numerical scheme for our GRMHD simulations are the same as those reported in [9, 20], to which the reader may refer for details. Here we briefly summarize the method and introduce our notation. We adopt geometrized units ($G = c = 1$) except where stated explicitly.

We use the 3+1 formulation of general relativity and decompose the metric into the following form:

$$ds^2 = -\alpha^2 dt^2 + \gamma_{ij}(dx^i + \beta^i dt)(dx^j + \beta^j dt). \quad (1)$$

The fundamental variables for the metric evolution are the spatial three-metric γ_{ij} and extrinsic curvature K_{ij} . We adopt the BSSN formalism [43, 44] to evolve γ_{ij} and K_{ij} . In this formalism, the evolution variables are the conformal exponent $\phi \equiv \ln \gamma/12$, the conformal 3-metric $\tilde{\gamma}_{ij} = e^{-4\phi}\gamma_{ij}$, three auxiliary functions $\tilde{\Gamma}^i \equiv -\tilde{\gamma}^{ij}{}_{,j}$, the trace of the extrinsic curvature K , and the tracefree part of the conformal extrinsic curvature $\tilde{A}_{ij} \equiv e^{-4\phi}(K_{ij} - \gamma_{ij}K/3)$. Here, $\gamma = \det(\gamma_{ij})$. The full spacetime metric $g_{\mu\nu}$ is related to the three-metric $\gamma_{\mu\nu}$ by $\gamma_{\mu\nu} = g_{\mu\nu} + n_\mu n_\nu$, where the future-directed, timelike unit vector n^μ normal to the time slice can be written in terms of the lapse α and shift β^i as $n^\mu = \alpha^{-1}(1, -\beta^i)$. As for the gauge conditions, we adopt an advective “1+log” slicing condition for the lapse and a second-order “non-shifting-shift” [33, 45] as in our BHNS simulations [20].

The BSSN equations are evolved with fourth-order accurate spatial differencing and upwinding on the shift advection terms. We apply Sommerfeld outgoing wave boundary conditions to all BSSN fields, as in [20]. Our code is embedded in the Cactus parallelization framework [46], whereby our second-order iterated Crank-Nicholson time-stepping is managed by the MoL, or method of lines, thorn. We use the moving puncture technique to handle any black hole that may form after the merger of the NSNS. The apparent horizon of the black hole is computed using the `ahfinderdirect` Cactus thorn [47]. Before an apparent horizon appears, we find that adding a Hamiltonian constraint term to the evolution equation of ϕ as in [48] leads to smaller constraint violation during the evolution. However, when a black hole appears, we remove this term as it sometimes leads to unstable evolution.

The fundamental variables in ideal MHD are the rest-mass density ρ_0 , specific internal energy ϵ , pressure P , four-velocity u^μ , and magnetic field B^μ measured by a normal observer moving with a 4-velocity n^μ (note that $B^\mu n_\mu = 0$). The ideal MHD condition is written as $u_\mu F^{\mu\nu} = 0$, where $F^{\mu\nu}$ is the electromagnetic (Faraday) tensor. The tensor $F^{\mu\nu}$ and its dual in the ideal MHD approximation are given by

$$F^{\mu\nu} = \epsilon^{\mu\nu\alpha\beta} u_\alpha b_\beta, \quad (2)$$

$$F_{\mu\nu}^* \equiv \frac{1}{2}\epsilon_{\mu\nu\alpha\beta} F^{\alpha\beta} = b_\mu u_\nu - b_\nu u_\mu, \quad (3)$$

where $\epsilon_{\mu\nu\alpha\beta}$ is the Levi-Civita tensor. Here we have introduced an auxiliary magnetic 4-vector $b^\mu = B_{(u)}^\mu/\sqrt{4\pi}$, where $B_{(u)}^\mu$ is the magnetic field measured by an observer comoving with the fluid and is related to B^μ by

$$B_{(u)}^\mu = -\frac{(\delta^\mu{}_\nu + u^\mu u_\nu)B^\nu}{n_\lambda u^\lambda}. \quad (4)$$

The energy-momentum tensor is written as

$$T_{\mu\nu} = T_{\mu\nu}^{\text{Fluid}} + T_{\mu\nu}^{\text{EM}}, \quad (5)$$

where $T_{\mu\nu}^{\text{Fluid}}$ and $T_{\mu\nu}^{\text{EM}}$ denote the fluid and electromagnetic contributions to the stress-energy tensor. They are given by

$$T_{\mu\nu}^{\text{Fluid}} = \rho_0 h u_\mu u_\nu + P g_{\mu\nu}, \quad (6)$$

and

$$\begin{aligned} T_{\mu\nu}^{\text{EM}} &= \frac{1}{4\pi} \left(F_{\mu\sigma} F_\nu{}^\sigma - \frac{1}{4} g_{\mu\nu} F_{\alpha\beta} F^{\alpha\beta} \right) \\ &= \left(\frac{1}{2} g_{\mu\nu} + u_\mu u_\nu \right) b^2 - b_\mu b_\nu, \end{aligned} \quad (7)$$

where $h \equiv 1 + \epsilon + P/\rho_0$ is the specific enthalpy, and $b^2 \equiv b^\mu b_\mu$. Hence, the total stress-energy tensor becomes

$$T_{\mu\nu} = (\rho_0 h + b^2) u_\mu u_\nu + \left(P + \frac{b^2}{2} \right) g_{\mu\nu} - b_\mu b_\nu. \quad (8)$$

In our numerical implementation of the GRMHD and magnetic induction equations, we evolve the densitized density ρ_* , densitized momentum density \tilde{S}_i , densitized energy density $\tilde{\tau}$, and densitized magnetic field \mathcal{B}^i . They are defined as

$$\rho_* \equiv -\sqrt{\gamma} \rho_0 n_\mu u^\mu, \quad (9)$$

$$\tilde{S}_i \equiv -\sqrt{\gamma} T_{\mu\nu} n^\mu \gamma_i{}^\nu, \quad (10)$$

$$\tilde{\tau} \equiv \sqrt{\gamma} T_{\mu\nu} n^\mu n^\nu - \rho_*, \quad (11)$$

$$\mathcal{B}^i \equiv \sqrt{\gamma} B^i. \quad (12)$$

During the evolution, we also need the three-velocity $v^i = u^i/u^t$.

The MHD and induction equations are written in conservative form for variables ρ_* , \tilde{S}_i , $\tilde{\tau}$, and \mathcal{B}^i and evolved using an HRSC scheme. Specifically, we use the monotized central (MC) scheme [49] for data reconstruction and the HLL (Harten, Lax and van-Leer) scheme [50] to compute the flux. The magnetic field \mathcal{B}^i has to satisfy the “no monopole” constraint $\partial_i \mathcal{B}^i = 0$. We adopt the flux-interpolated constrained transport (flux-CT) scheme [51, 52] to impose this constraint. In this scheme, the induction equation is differenced in such a way that a second order, corner-centered representation of the divergence is preserved as a numerical identity.

At each timestep, the hydrodynamic “primitive” variables (ρ_0, P, v^i) must be computed from the “conservative” variables $(\rho_*, \tilde{\tau}, \tilde{S}_i)$. This is done by numerically solving the algebraic equations (9)–(11) together with an EOS $P = P(\rho_0, \epsilon)$. In this paper, we adopt a Γ -law EOS, $P = (\Gamma - 1)\rho_0\epsilon$, with $\Gamma = 2$.

As in many hydrodynamic simulations in astrophysics, we add a tenuous “atmosphere” that covers the computational grid outside the star. The atmospheric rest-mass density is set to $10^{-10}\rho_{\max}(0)$, where $\rho_{\max}(0)$ is the initial maximum rest-mass density of the stars. As in [15], we apply outer boundary conditions on the primitive variables ρ, P, v^i , and B^i . Outflow boundary conditions are imposed on the hydrodynamic variables, and the magnetic field is linearly extrapolated onto the boundaries. Finally, the evolution variables ρ_*, \tilde{S}_i , and $\tilde{\tau}$ are recomputed on the boundary.

Our GRMHD code (DLSS) has been thoroughly tested by passing a robust suite of tests. These tests include maintaining stable rotating stars in stationary equilibrium, reproducing the exact Oppenheimer-Snyder solution for collapse to a black hole, and reproducing analytic solutions for MHD shocks, nonlinear MHD wave propagation, magnetized Bondi accretion, and MHD waves induced by linear gravitational waves [9]. Our DLSS code has also been compared with SS’s GRMHD code [10] by performing identical simulations of the evolution of magnetized hypermassive NSs [13, 15] and of magnetorotational collapse of stellar cores [16]. We obtain good agreement between these two independent codes. Our code has also been used to study the collapse of very massive, magnetized, rotating stars to black hole [21], evolution of merging BHBH [53] and BHNS binaries [20], and the evolution of relativistic hydrodynamic matter in the presence of puncture black holes [54]. Recently, our code has been generalized to incorporate (optically thick) radiation transport and its feedback on hydrodynamic matter [55].

B. Initial data

We adopt the same irrotational, quasi-circular NSNS initial data as in [1]. These initial data set were generated by Taniguchi & Gourgoulhon [56, 57] by numerically solving the constraint equations of general relativity in the CTS framework. We consider three models studied in [1]: M1414, M1616 and M1418.

All models assume an $n=1$ polytropic EOS for the neutron stars: $P = \kappa\rho_0^2$. The compaction, $(M_*/R)_\infty$, is defined as the ratio of the ADM (Arnowitt-Deser-Misner) mass M_* to the areal radius R of a spherical neutron star in isolation. For an $n=1$ polytropic EOS, the compaction uniquely specifies the neutron star. We thus label the NSNS models by the compaction of each neutron star. Model M1418 means the compactness of the two neutron stars are 0.14 and 0.18. Hence the two neutron stars do not have the same rest masses. For models M1414 and

M1616, the two neutron stars are of equal rest mass and their compactness are 0.14 (for model M1414) and 0.16 (for model M1616). It is convenient to rescale all quantities with respect to κ . Since $\kappa^{1/2}$ has dimensions of length, we can define the nondimensional variables [58] $\bar{M} = \kappa^{-1/2}M$, $\bar{R} = \kappa^{-1/2}R$, and $\bar{\rho}_0 = \kappa\rho_0$. Here M is the ADM mass of the binary. The relationship between these nondimensional variables and quantities in cgs units are

$$M = 10M_\odot \left(\frac{\kappa}{1.455 \times 10^5 \text{cgs}} \right)^{1/2} \bar{M} \quad (13)$$

$$R = 14.8 \text{km} \left(\frac{\kappa}{1.455 \times 10^5 \text{cgs}} \right)^{1/2} \bar{R} \quad (14)$$

$$\rho_0 = 6.18 \times 10^{15} \text{gcm}^{-3} \left(\frac{\kappa}{1.455 \times 10^5 \text{cgs}} \right) \bar{\rho}_0, \quad (15)$$

where the value $\kappa = 1.455 \times 10^5 \text{cgs}$ is used by [59]. The maximum rest mass for a spherical neutron star for this EOS is $\bar{M}_0^{(\text{TOV})} = 0.180$, and the maximum ADM mass is $\bar{M}_*^{\text{max}} = 0.164$. Table I summarizes the characteristics of our models.

To study the effects of magnetic fields, we add a small poloidal magnetic field to the quasi-equilibrium model. We orient our coordinates so that the initial maximum densities of the two neutron stars are located at $(x_1, 0, 0)$ and $(x_2, 0, 0)$ with $x_1 < 0$ and $x_2 > 0$. For each neutron star l , we specify the magnetic vector potential

$$A_x^{(l)} = -(y/\varpi_l^2)A_\varphi^{(l)}, \quad A_y^{(l)} = (x/\varpi_l^2)A_\varphi^{(l)}, \quad (16)$$

$$A_z^{(l)} = 0, \quad (l = 1, 2) \quad (17)$$

where $\varpi_l \equiv \sqrt{(x - x_l)^2 + y^2}$ and we set

$$A_\varphi^{(l)} = A_b \varpi_l^2 \left(1 - \frac{\rho_0}{\rho_0^{\text{max}}} \right)^{n_p} \max(P - P_{\text{cut}}, 0). \quad (18)$$

Here A_b , n_p and P_{cut} are free parameters. The magnetic field in the l -th neutron star is then computed by $B_{(l)}^i = n_\mu \epsilon^{\mu i j k} \partial_j A_k^{(l)}$. This guarantees that the magnetic constraint $\partial_j \mathcal{B}^j = 0$ is automatically satisfied. The parameter A_b determines the strength of the B-field. The cutoff pressure parameter P_{cut} confines the B-field inside the neutron star to reside within $P > P_{\text{cut}}$. The parameter n_p shifts the location of the maximum B-field in the star. A larger value of n_p results in the maximum B-field located in the lower density region of the star. In this paper, we set P_{cut} to be 4% or 0.1% of the maximum pressure, $n_p = 0$ or 3, and set A_b so that the volume-averaged magnetic field is $10^{16} \text{G} (M_0/2.8M_\odot)$, where M_0 is the total rest mass of the stars. There is no initial exterior magnetic field. Figure 1 shows the initial magnetic field configurations for a widely separated NS companion with compaction $M_*/R = 0.14$. The magnetic field lines, as well as density distribution, for each NS in our binary at $t = 0$ are slightly distorted from those shown in Fig. 1 due to tidal effects. Table II lists the simulations performed in this paper with a brief summary of

TABLE I: Irrotational, quasiequilibrium NSNS models in circular orbit. Here $(M_*/R)_\infty$ is the neutron star compaction, $\bar{\rho}_0^{\max}$ is the maximum nondimensional rest-mass density of a neutron star, \bar{M}_0 is the nondimensional total rest mass of the binary, \bar{M} is the nondimensional ADM mass of the system, J is the ADM angular momentum, $q = M_0^{(1)}/M_0^{(2)}$ is the ratio of the rest masses of the stars, Ω_0 is the quasi-circular orbital angular velocity, and $P_0 = 2\pi/\Omega_0$ is the orbital period.

Model	$(M_*/R)_\infty$	$\bar{\rho}_0^{\max}$	\bar{M}_0	\bar{M}	J/M^2	q	$M\Omega_0$	P_0/M
M1414	0.14, 0.14	0.118, 0.118	0.292	0.269	0.951	1.00	0.0326	193
M1616	0.16, 0.16	0.151, 0.151	0.320	0.292	0.914	1.00	0.0395	158
M1418	0.14, 0.18	0.118, 0.195	0.317	0.290	0.933	0.855	0.0345	182

TABLE II: Parameters and results of various runs. The label HNS stands for “hypermassive neutron star,” BH stands for “black hole,” M_0^{disk} is the rest mass of the disk around the black hole, and J_H/M_H^2 is the spin parameter of the black hole.

Run	Model	B-field	n_p	$P_{\text{cut}}/P_{\text{max}}$	Result	M_0^{disk}/M_0	J_H/M_H^2
M1414B0	M1414	no	—	—	HNS	—	—
M1414B1		yes	0	0.04	HNS	—	—
M1616B0	M1616	no	—	—	BH	$< 10^{-6}$	≈ 0.85
M1616B1		yes	0	0.04	BH	$< 10^{-4}$	≈ 0.85
M1616B2		yes	3	0.001	BH	$< 2 \times 10^{-4}$	≈ 0.85
M1418B0	M1418	no	—	—	BH	≈ 0.013	≈ 0.8
M1418B1		yes	0	0.04	BH	$\lesssim 0.018$	≈ 0.8

the outcomes. We note that Anderson et al. [28] also set up the magnetic fields in a very similar way. Their setup corresponds to setting the parameters $n_p=0$, P_{cut} to the atmosphere value, and A_b such that the maximum B-field strength in each NS is $9.6 \times 10^{15} \text{G} (1.78 M_\odot/M)$.

We note that the interior magnetic field strength of 10^{16}G is large compared to values inferred for the surface of a typical pulsar ($B \sim 10^{12} \text{G}$), but it is comparable to the strength in a magnetar [34]. We find that for this B-field strength, the magnetic pressure, $P_{\text{mag}} = b^2/2$, is about 0.1% of the gas pressure, and the total magnetic energy is $\sim 10^{-5}$ of the ADM mass. We note that the accuracy of the ADM mass of our CTS initial data is also of order 10^{-5} [56]. Hence, adding a B-field of this strength induces negligible constraint violation and causes only a small perturbation to the equilibrium of the stars and their orbit. In addition, the magnetic field profile inside a neutron star is not known. Our profile is to make the ratio P_{mag}/P small initially in most regions. As a result, the magnetic field introduces only a small perturbation to the fluid and no “magnetic wind” is generated in the low-density regions of the star.

In nature, magnetic fields are not confined inside the NS, but extend out to the NS exterior. The exterior fields of the two NSs in the binary will interact and modify the dynamics during the inspiral phase. This effect has been studied analytically in Newtonian and post-Newtonian calculations in [60, 61, 62]. As a rough estimate, we approximate the NS by a sphere of radius R . Consider a pure dipole exterior field and a nearly uniform interior field aligned with the orbital angular momentum. The magnetic dipole moment μ is related to the interior field strength B by $\mu \approx BR^3/2$. The accumulated gravitational wave cycles during the inspiral phase from grav-

itational wave frequencies f_{\min} to f_{\max} due to magnetic dipole interaction is estimated to be [60]

$$\delta N_{\text{mag}} \sim -\frac{25}{64\pi} \frac{B_1 B_2 R_1^3 R_2^3}{\eta^2 M^4} (\pi M f)^{-1/3} \Big|_{f_{\min}}^{f_{\max}}, \quad (19)$$

where $\eta = M_1 M_2 / (M_1 + M_2)^2$ is the symmetric mass ratio of the two NSs. To estimate the upper bound starting from our initial data, we set $f_{\max} = \infty$ and f_{\min} to twice of the initial orbital frequency of the binaries in our models. We find $\delta N_{\text{mag}} < 0.02$ for all three models. Hence the effect of magnetic dipole interaction during the inspiral phase is negligible, even assuming our large adopted field strength. For this reason, any appreciable dynamical effects of the magnetic fields will occur only during and after the merger phase, for which our confined field model will be adequate.

C. Grid setup

Even though the dynamics of the system is mainly concentrated in the central region with radius $r \lesssim 10M$, we set our computational grid to $r \approx 50M$ in order to extract gravitational radiation. To reduce computational resources, we employ fisheye coordinates [63, 64] to allocate the grid more effectively. Fisheye coordinates \bar{x}^i are related to the original coordinates x^i through the following transformation:

$$x^i = \frac{\bar{x}^i}{\bar{r}} r(\bar{r}), \quad (20)$$

$$r(\bar{r}) = a\bar{r} + \frac{(1-a)s}{2 \tanh(\bar{r}_0/s)} \ln \frac{\cosh[(\bar{r} + \bar{r}_0)/s]}{\cosh[(\bar{r} - \bar{r}_0)/s]}, \quad (21)$$

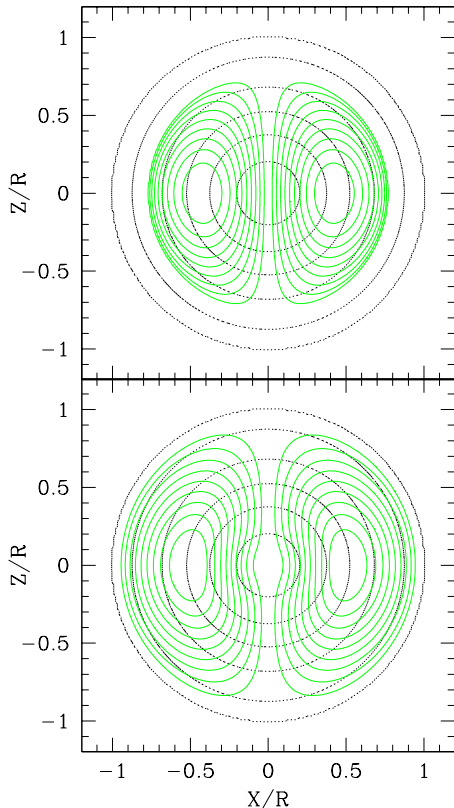


FIG. 1: Magnetic field configurations in a widely separated, spherical NS companion constructed from the vector potential in Eq. (18) for $n_p=0$ and $P_{\text{cut}}=0.04P_{\text{max}}$ (upper panel), and for $n_p=3$ and $P_{\text{cut}}=0.001P_{\text{max}}$ (lower panel). Here P_{max} is the maximum pressure. The compaction of this NS is $M_*/R=0.14$. Dotted (black) concentric circles are rest-mass density contours drawn for $\rho_0/\rho_0^{\text{max}} = 0.9, 0.7, 0.5, 0.3, 0.1$ and 0.001 . Solid (green) lines are contours of A_φ , which coincide with the magnetic field lines in axisymmetry. Contour levels of A_φ are drawn for $A_\varphi = (A_\varphi^{\text{max}} - A_\varphi^{\text{min}})(i/10)^2 + A_\varphi^{\text{min}}$ with $i=1, 2, \dots, 9$, where A_φ^{max} and A_φ^{min} are the maximum and minimum value of A_φ , respectively.

where $r = \sqrt{x^2 + y^2 + z^2}$, $\bar{r} = \sqrt{\bar{x}^2 + \bar{y}^2 + \bar{z}^2}$. The quantities a , \bar{r}_0 and s are constant parameters, which are set to $a = 3$, $\kappa^{-1/2}\bar{r}_0=2.4$, and $\kappa^{-1/2}s=0.6$ in all of our simulations. With this choice, the grid spacing in the region $\kappa^{-1/2}r > 2.4$ is increased by a factor of 3.

We use a cell-centered grid with size $2N \times 2N \times N$ in \bar{x} - \bar{y} - \bar{z} (assuming equatorial symmetry), covering a computational domain $\bar{x} \in (-N\Delta, N\Delta)$, $\bar{y} \in (-N\Delta, N\Delta)$, and $\bar{z} \in (0, N\Delta)$. Here N is an integer, Δ is the grid spacing and \bar{z} is the rotation axis. We set $N = 150$, $\kappa^{-1/2}\Delta = 0.04$ for models M1414 and M1616, and $N = 200$, $\kappa^{-1/2}\Delta = 0.03$ for models M1418. These values of Δ are chosen so that the diameter of each neutron star in the equatorial plane is covered by $\gtrsim 40$ grid points. This is the same resolution used in [1]. We have performed a simulation with 75% of the grid spacing (but with closer outer boundary) for the unmagnetized M1414 case and find that the result is very close to our standard

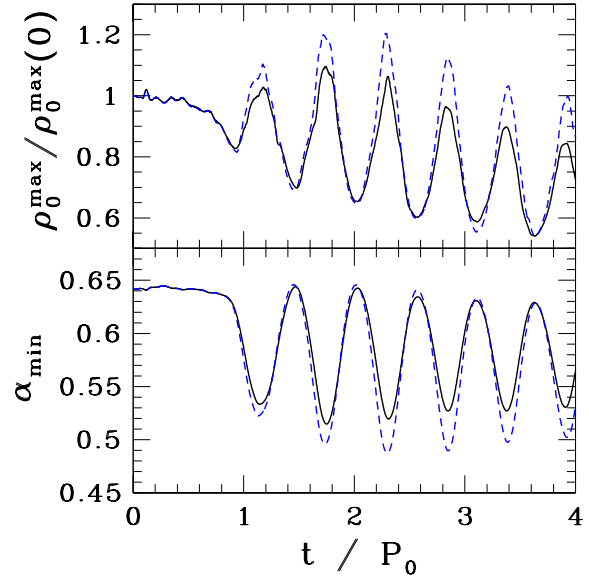


FIG. 2: Evolution of maximum density ρ_0^{max} and minimum lapse α_{min} for unmagnetized (black solid line) and magnetized (blue dash line) runs of model M1414. The time t is normalized by the initial orbital period $P_0=193M=1.3 \times 10^{-5}s (M_0/2.8M_\odot)$. The initial maximum rest-mass density is $\rho_0^{\text{max}}(0)=0.118/\kappa=7.9 \times 10^{14} \text{ g cm}^{-3} (2.8M_\odot/M_0)^2$. The merger occurs at $t \approx 1P_0$.

resolution.

III. RESULTS

A. Model M1414

Model M1414 is an equal-mass NSNS binary. The total rest mass of the system is $M_0 = 1.6M_0^{\text{(TOV)}}$. In the absence of magnetic field (run M1414B0), the neutron stars merge after about one orbit ($\approx 190M$), consistent with the result in [1]. We find that magnetic field does not change the result. After the merger, the star becomes a hypermassive NS. Figure 2 shows the evolution of maximum density ρ_0^{max} and minimum lapse α_{min} for both unmagnetized and magnetized cases. Figure 3 shows the density profile along the x -axis and y -axis in the equatorial plane at three different times. We see that the unmagnetized case is very close to the simulation in [1] (see their Fig. 6a and Fig. 7b).

Figures 4 and 5 show the density contours and velocity field in the equatorial plane. We see that magnetic field causes some mass-shedding in the low-density region. After the merger, we see double cores rotating around the center, as in [1]. The star is also pulsating with a large amplitude (see Figs. 2 and 3). These motions give rise to gravitational wave signals after the merger (see below). We note that the apparent bar-like structure seen in Figs. 4 and 5 in some of the density contours at late

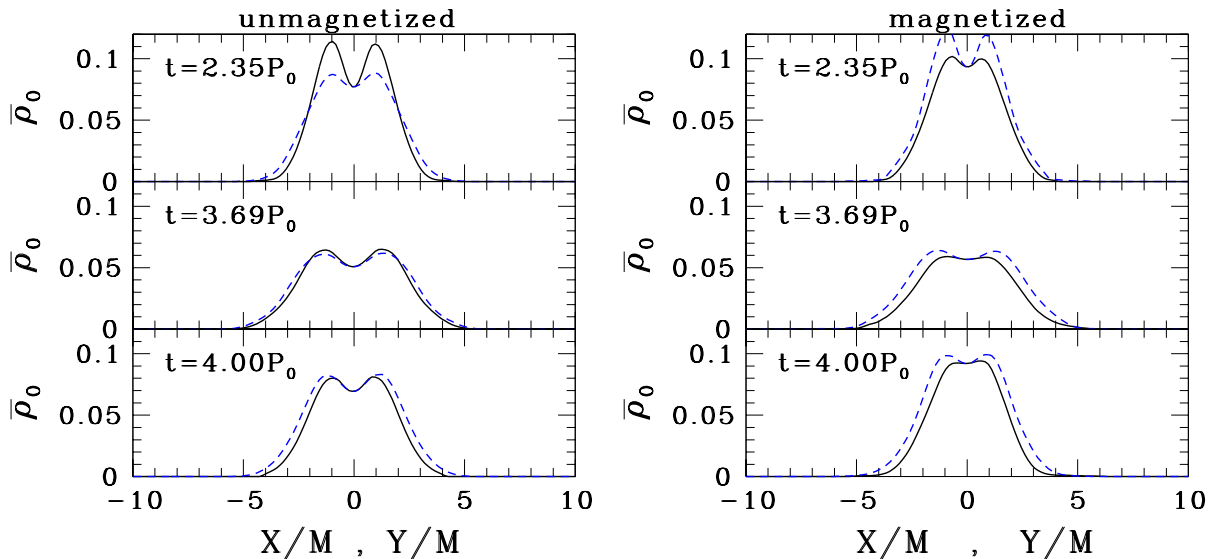


FIG. 3: Nondimensional rest-mass density $\bar{\rho}_0 = \kappa\rho_0$ along the x -axis (black solid lines) and y -axis (blue dash lines) in the equatorial plane at three different times for the unmagnetized (left) and magnetized (right) cases.

times is a coordinate (gauge) artifact. In our coordinates, the bar is nonrotating and stationary for several periods. Figure 6 shows the contours of constant geodesic proper distance from the center of the grid. (The geodesic proper distance between P and Q in a spatial slice is defined as the proper length of the (spatial) geodesic joining P and Q). We have verified that the bar-like density contours roughly coincide with the constant geodesic proper distance contours, indicating that the density distribution in the bar-like region is actually close to axisymmetric.

Magnetic fields do not affect the dynamics of the system prior to merger, as expected. After the merger, we see a larger amplitude of pulsation in the magnetized case. However, we expect that the main effects of the magnetic field occur on a longer (secular) timescale when the field is amplified by differential rotation. Magnetic winding will occur on an Alfvén timescale $t_A \sim R/v_A \sim 10$ rotation periods, where $v_A = \sqrt{b^2/(\rho_0 h + b^2)}$ is the Alfvén velocity. Additional amplification will be triggered by the magnetorotational instability (MRI) [13, 15]. This amplification will lead to transport of angular momentum and may trigger a ‘delayed’ collapse [13, 15]. We do not follow the evolution for that long in this paper. We note that the grid resolution in our simulation is insufficient to resolve some of the MHD instabilities such as the MRI [3]. However, our current resolution is adequate to capture the main effects of magnetic fields on our simulation timescale (a few oscillation periods after the merger). We note, however, that we have already performed high-resolution simulations in axisymmetry to study the long-term secular evolution of magnetized hypermassive NS remnants [13, 15]. We con-

firm that the magnetic fields cause transport of angular momentum, resulting in a delayed collapse of the star to a black hole surrounded by a hot, massive disk.

Figure 7 shows the gravitational waveforms for both the magnetized and unmagnetized cases. We compute the $l = 2$, $m = 2$, $s = -2$ spin-weighted spherical harmonics of the Weyl tensor ψ_4 at three radii $32M$, $38M$, and $43M$. As shown in Fig. 7a and 7b, the computed ψ_4^{22} at these three radii are hardly distinguishable when properly scaled, indicating that the extracted waveforms are being measured in the wave zone and are reliable. We see again that the waveforms of the magnetized and unmagnetized cases show negligible differences before the merger. After the merger, the magnetic field significantly affects the motion of the fluid, and the waveforms exhibit observable differences in both the amplitude and phase. Notice that there are still gravitational wave signals after the merger. This is mainly caused by the rotation of the double cores and the pulsation of the merged remnant.

Figures 8 and 9 show the L2 norms of the Hamiltonian and momentum constraint violations. The L2 norms are normalized as in [20]. We see that the constraint violations are less than 5% during the entire simulations ($4P_0 = 772M$).

B. Model M1616

Model M1616 is also an equal-mass NSNS binary. The total rest mass of the system is $M_0 = 1.78M_0^{(\text{TOV})}$. In the absence of magnetic field, the system merges at $t \approx 150M$ ($\approx 0.9P_0$) and the star promptly collapses to a black

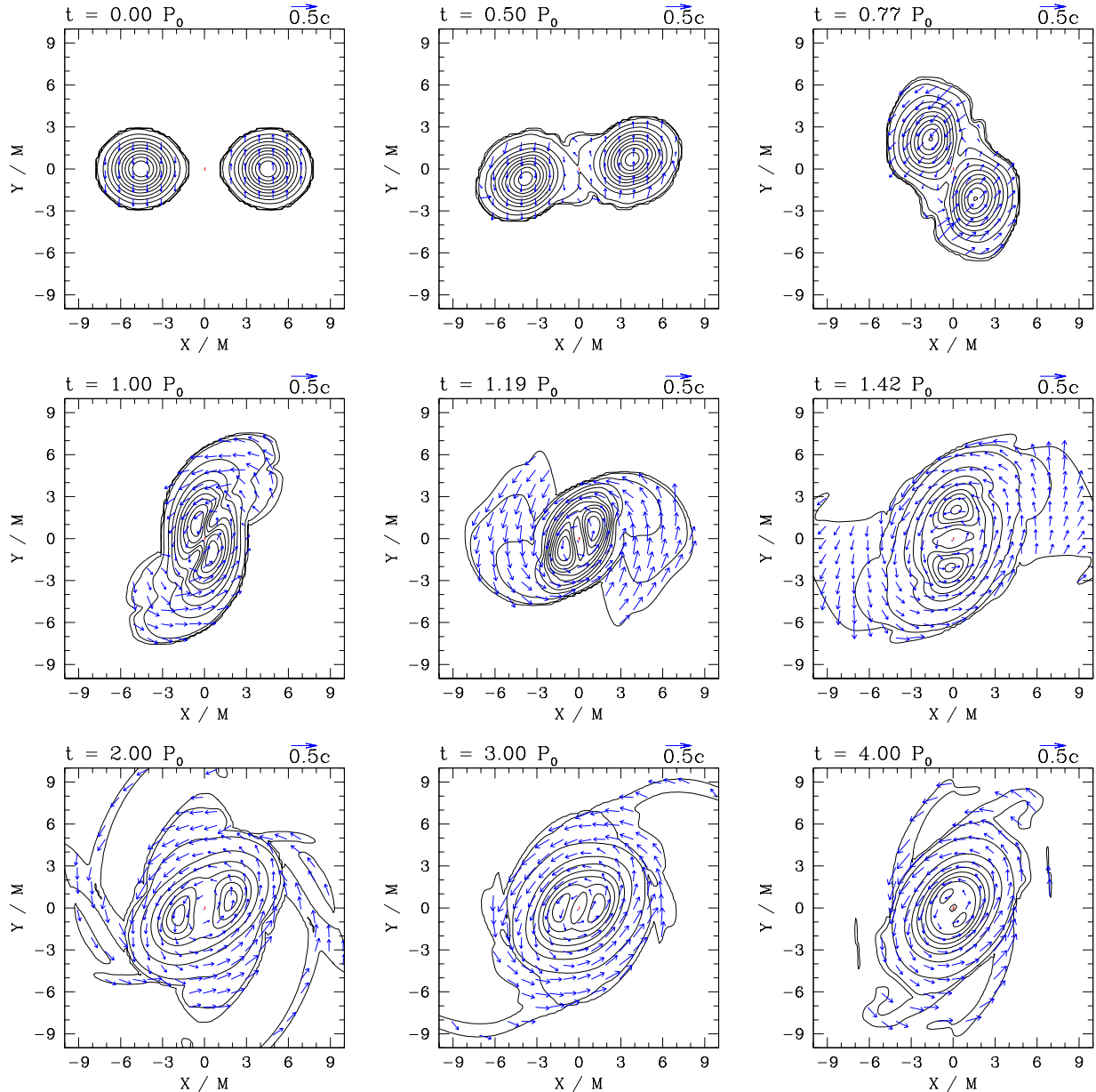


FIG. 4: Snapshots of density and velocity field in the equatorial plane from run M1414B0 (unmagnetized run). Density contours are drawn for $\rho_0/\rho_0(0)=0.9, 0.8, 0.7, 0.6, 0.5, 0.4, 0.3, 0.2, 0.1, 0.01, 0.001$, and 0.0001 .

hole. An apparent horizon forms at $t = 192M$. Figure 10 shows the evolution of the maximum density ρ_0^{\max} and minimum lapse α_{\min} . Figure 11 shows snapshots of the equatorial density contours and velocity field. Our result again agrees with [1]. The simulation in [1] is terminated soon after the formation of an apparent horizon because of the grid stretching. Hence [1] can only give an estimate of the upper bound of $0.002M_0$ for the amount of material that can form a disk. We are able to use the puncture technique to continue the evolution until the system settles down to a stationary state. Figure 14 shows the rest mass of the material outside the apparent horizon M_{out} . We see that all the material falls into the

black hole. The small residual value of $M_{\text{out}} \approx 10^{-6}M_0$ at late times is due to the presence of our (artificial) atmosphere. After $t > 250M$, the system settles down to a vacuum rotating Kerr black-hole spacetime.

We perform two simulations for the magnetized cases with different initial magnetic field profiles (see Table II). Run M1616B1 has the same profile as M1414B1. In run M1616B2, more magnetic field is placed in the outer layers of the neutron stars, and hence it could counteract the gravitational pull of the black hole more effectively. We see from Fig. 10 that runs M1414B1 and M1616B2 are qualitatively the same as run M1616B0 (unmagnetized run). They both collapse promptly to a black

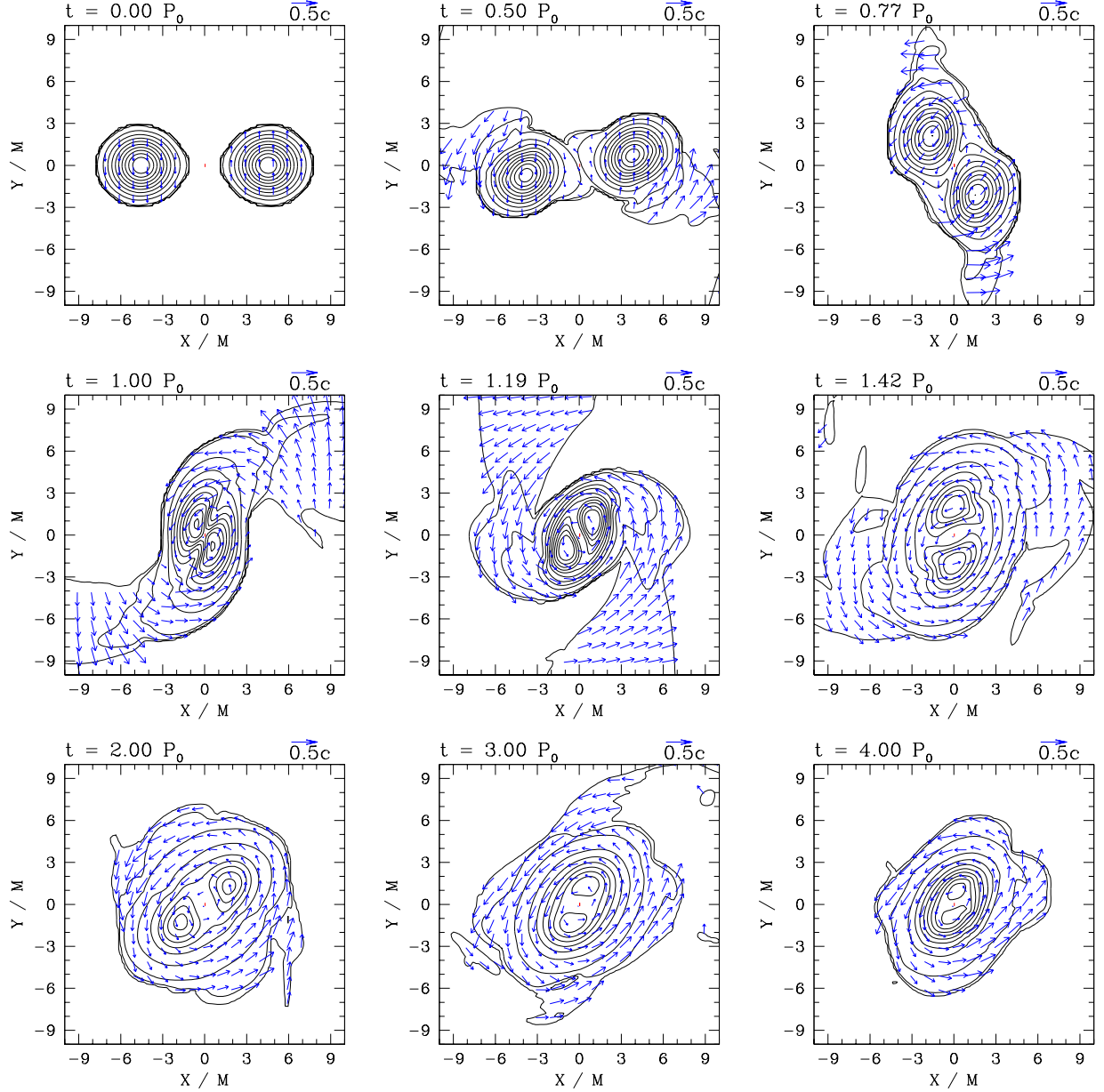


FIG. 5: Same as Fig. 4 but for run M1414B1 (magnetized run).

hole. The apparent horizon appears at about the same time ($t = 192M$) in all three cases. Figures 12 and 13 show snapshots of equatorial density contours and velocity field. In Fig. 14, we see that $M_{\text{disk}}/M_0 \lesssim 10^{-4}$ for both M1616B1 and M1616B2. We see that magnetic fields cause a substantial delay in the time at which material in the low-density region falls into the black hole. The effect is more pronounced for the case M1616B2 when more magnetic field is in the low-density region. The simulations of M1616B1 and M1616B2 are terminated at $t \approx 500M$ when constraint violations start to become large (see Fig. 18). However, our current results already indicate that even in the presence of magnetic fields the

amount of material outside the black hole is very small.

Figure 15 shows the gravitational waveforms for all M1616 models. We see that the waveforms for the three runs are very close. This is expected because magnetic fields can affect the dynamics substantially only well after the merger. However, the merged remnants quickly collapse to black holes before the magnetic fields have enough time to change the fluid's motion significantly. We do see, however, that the amplitude of the waves during the collapse are slightly larger for the magnetized cases. Figure 16 shows the two polarizations h_+ and h_\times of run M1616B0 as observed in the direction 45° to the z -axis.

Figures 17 and 18 show the L2 norms of the constraint

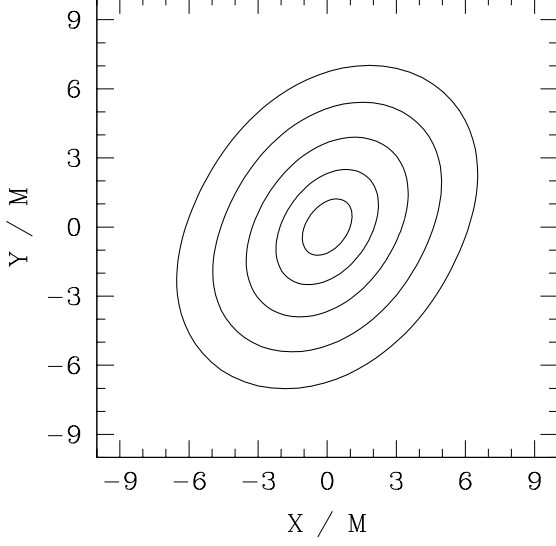


FIG. 6: Constant geodesic proper distance from the center, D , in the equatorial plane at $t = 4P_0$ for run M1414B0. Contours are drawn for $D/M = 1.86i$ ($i = 1, 2, 3, 4, 5$).

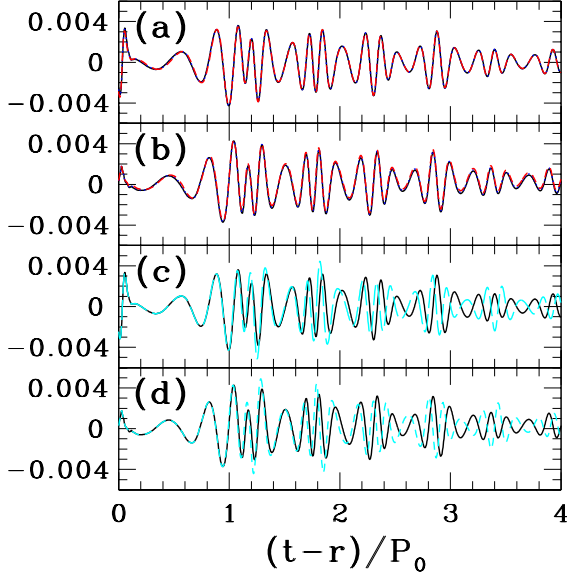


FIG. 7: Gravitation waveforms for model M1414. (a) $\text{Re}(rM\psi_4^{22})$ extracted at $r = 43M$ (black solid line), $r = 38M$ (blue dotted line), and $r = 32M$ (red dash line). (b) Same as (a) but for $\text{Im}(rM\psi_4^{22})$. (c) $\text{Re}(rM\psi_4^{22})$ extracted at $r = 43M$ for the unmagnetized (black solid line) and magnetized (cyan dash line) cases. (d) Same as (c) but for $\text{Im}(rM\psi_4^{22})$. Note that in (a) and (b), the lines are hardly distinguishable, showing good agreement of waveforms at various extraction radii.

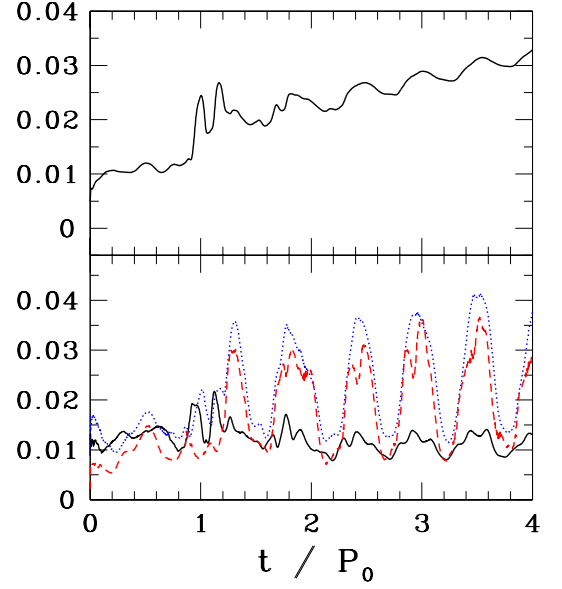


FIG. 8: Constraint violations for the unmagnetized run of model M1414. Upper panel: Normalized L2 norm of the Hamiltonian constraint. Lower panel: Normalized L2 norm of the x (black solid line), y (blue dotted line) and z (red dash line) components of the momentum constraint.

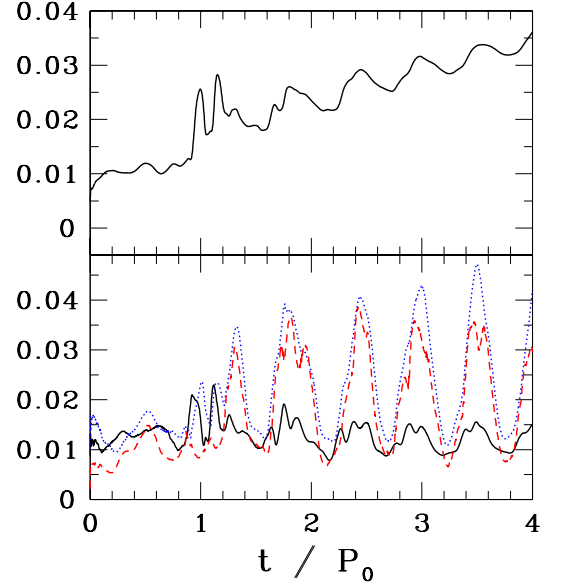


FIG. 9: Same as Fig. 8 but for the magnetized run of model M1414.

violations for runs M1616B0 and M1616B1. The plots for M1616B2 are similar to those of M1616B1 and so are not shown here. The peaks at $t = 192M$ are due to the formation of a central singularity and are contained inside the event horizon. After the apparent horizon appears at $t = 192M$, the constraints are computed only in the region outside the apparent horizon, and we see the

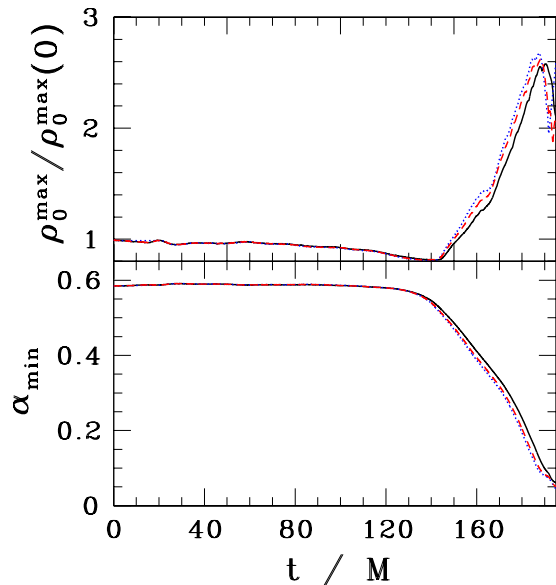


FIG. 10: Evolution of maximum density ρ_0^{\max} and minimum lapse α_{\min} for runs M1616B0 (black solid line), M1616B1 (blue dotted line) and M1616B2 (red dash line). The merger occurs at $t \approx 150M$, and an apparent horizon appears at $t = 192M$ for both magnetized and unmagnetized cases.

constraint violations drop to much lower values. This result confirms that the large constraint violations in the strong-field region are trapped inside the event horizon. For run M1616B0, the constraint violations are less than 3% most of the time. For run M1616B1, the momentum constraint violations are less than 5% most of the time. The Hamiltonian constraint violation is less than 5% before the collapse, around 5%–10% after the apparent horizon forms, and gradually increases to 12% at $t = 500M$, after which the simulation is terminated.

C. Model M1418

For model M1418, the ratio of the rest masses of the neutron stars are $q = M_0^{(1)}/M_0^{(2)} = 0.855$. The total rest mass of the system is $M_0 = 1.76M_0^{(\text{TOV})}$, which is about the same as model M1616. As in model M1414, we perform an unmagnetized (run M1418B0) and a magnetized (run M1418B1) simulation. The merger occurs at $t \approx 180M \approx 1P_0$. The merged remnant collapses to a black hole. An apparent horizon forms at $t = 232M$ for both cases. Figure 19 shows the evolution of the maximum density ρ_0^{\max} and minimum lapse α_{\min} . Figures 20 and 21 show snapshots of equatorial density contours and the velocity vector field.

Figure 22 shows the rest mass of the material outside the apparent horizon M_{out} . We see that for the unmagnetized case, M_{out}/M_0 is settling down to an equilibrium value ≈ 0.013 , which is consistent with the upper bound

0.04 reported in [1]. The simulation is terminated at $t \approx 450M$ since the constraint violations outside the apparent horizon increase to more than 15% and so the evolution becomes inaccurate. We suspect that the problem can be solved by increasing the grid resolution near the central singularity. We plan to investigate this issue in the near future. For the magnetized case, M_{out}/M_0 drops to 0.018 at the end of our simulation. The simulation is terminated at $t \approx 380M$ when the constraint violations exceed 15%. The magnetized run is qualitatively very similar to unmagnetized run at this stage. Unlike model M1616, however, there is a substantial amount of material left to form a disk in this case. Magnetic fields are expected to play an important role in the subsequent secular evolution of the disk. The field could drive MHD turbulence and generate ultra-relativistic jets. However, the disk mass is probably not large enough to produce a short-hard GRB in this case [65]. We have already studied axisymmetric, magnetized disk evolution around black holes in [42].

Figure 23 shows the gravitational waveforms. We see that the waveforms of the unmagnetized and magnetized simulations are very close, as we have found for model M1616.

IV. SUMMARY

We have performed a series of new simulations involving the coalescence of NSNS binaries in full general relativity, using the CTS quasiequilibrium NSNS initial data. We considered three models M1414, M1616 and M1418 previously studied by Shibata, Taniguchi & Uryū [1]. We performed unmagnetized and magnetized simulations for each model.

We find that our results for the unmagnetized runs agree with those in [1]. In particular, the remnant of the merger is a hypermassive neutron star for model M1414, a rotating black hole with negligible disk for model M1616, and a black hole surrounded by a disk with a rest mass less than 2% of the total rest mass of the system for model M1418. Given our good agreement with the results of Shibata, Taniguchi & Uryū [1] for unmagnetized binaries, the results of Anderson et al. [27, 28] remain somewhat puzzling for such configurations. Our simulations on magnetized NSNSs indicate that the magnetic fields can cause observable differences in the dynamics and gravitational waveforms after the merger (especially for model M1414). However, we find that the magnetic effects are less significant than those reported in [28].

For model M1414, the merged remnant consists of a double core rotating around the center, and the star pulsates. The motion in this remnant emits gravitational radiation. We see observable difference between the magnetized and unmagnetized cases in the amplitude of the pulsations. Gravitational waveforms also show differences in amplitude and phase after the merger. We expect that

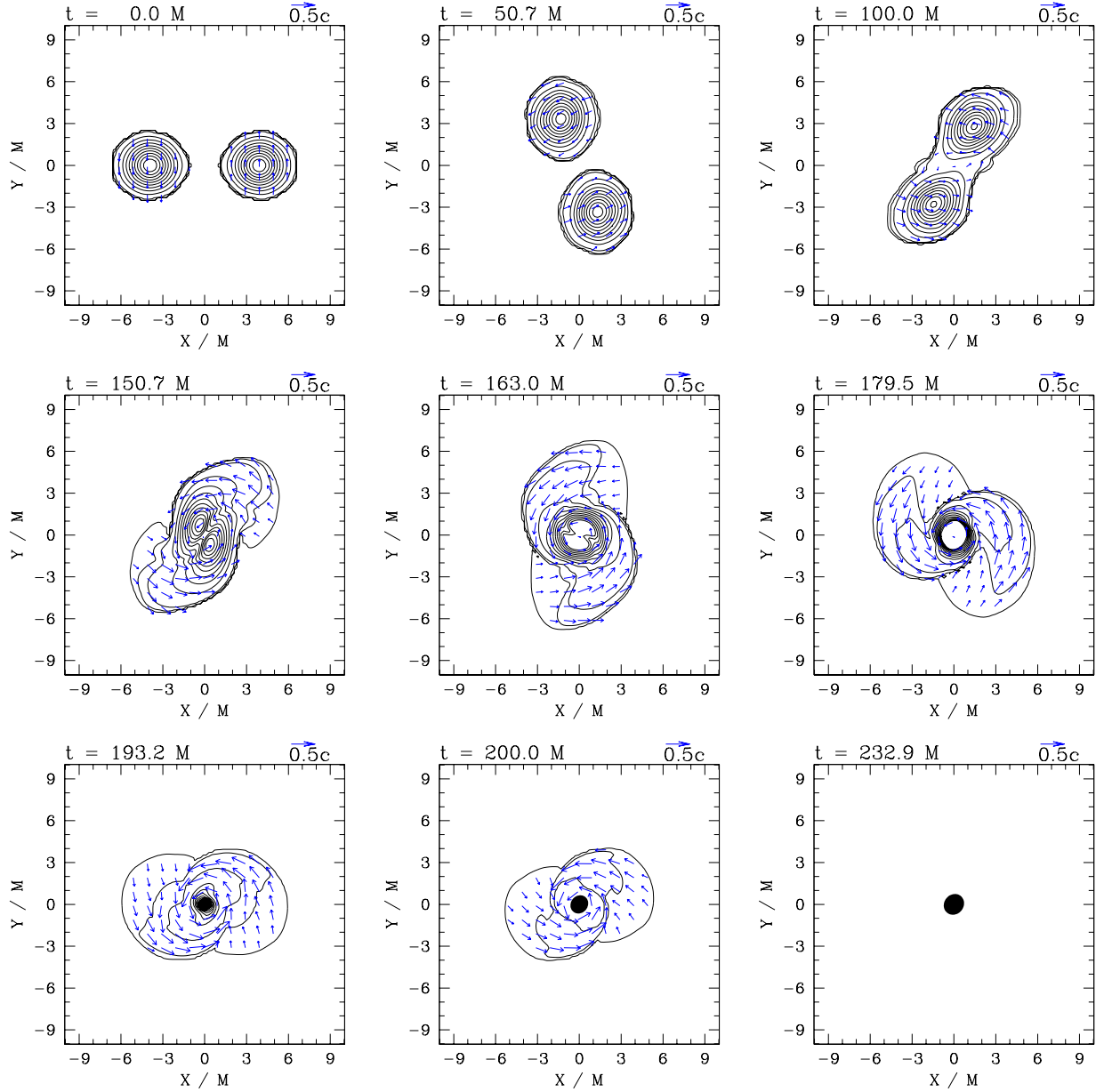


FIG. 11: Same as Fig. 4 but for run M1616B0 (unmagnetized run). The black region near the center in the last three panels denotes the apparent horizon.

the magnetic field will be amplified by differential rotation on a (secular) timescale of ~ 10 rotation periods.

For the more massive model M1616, prompt collapse to a black hole occurs following the merger. For the unmagnetized case, all the material falls into the black hole. For the magnetized cases, we try two different initial magnetic-field profiles and find that the final result is about the same as the unmagnetized case. We find that $\lesssim 10^{-4}$ of the total rest mass resides outside the black hole at the end of our simulations ($500M$). We see only a slight difference in the amplitude of the gravitational radiation between the magnetized and unmagnetized cases during the collapse.

For model M1418 consisting of unequal masses, the merged remnant also collapses promptly to a black hole after the merger, but there is a substantial amount of material left to form a disk. We find that the disk mass is $\lesssim 0.013M_0$ for the unmagnetized case and $\lesssim 0.018M_0$ for the magnetized case, where M_0 is the total rest mass of the system. Magnetic fields are crucial for the subsequent, secular evolution of the disk. We have previously performed long-term, axisymmetric simulations of magnetized disks around black holes resulting from the collapse of hypermassive neutron stars [42]. We find that the magnetic fields can cause outflows, depending on the EOS and the magnetic field configuration.

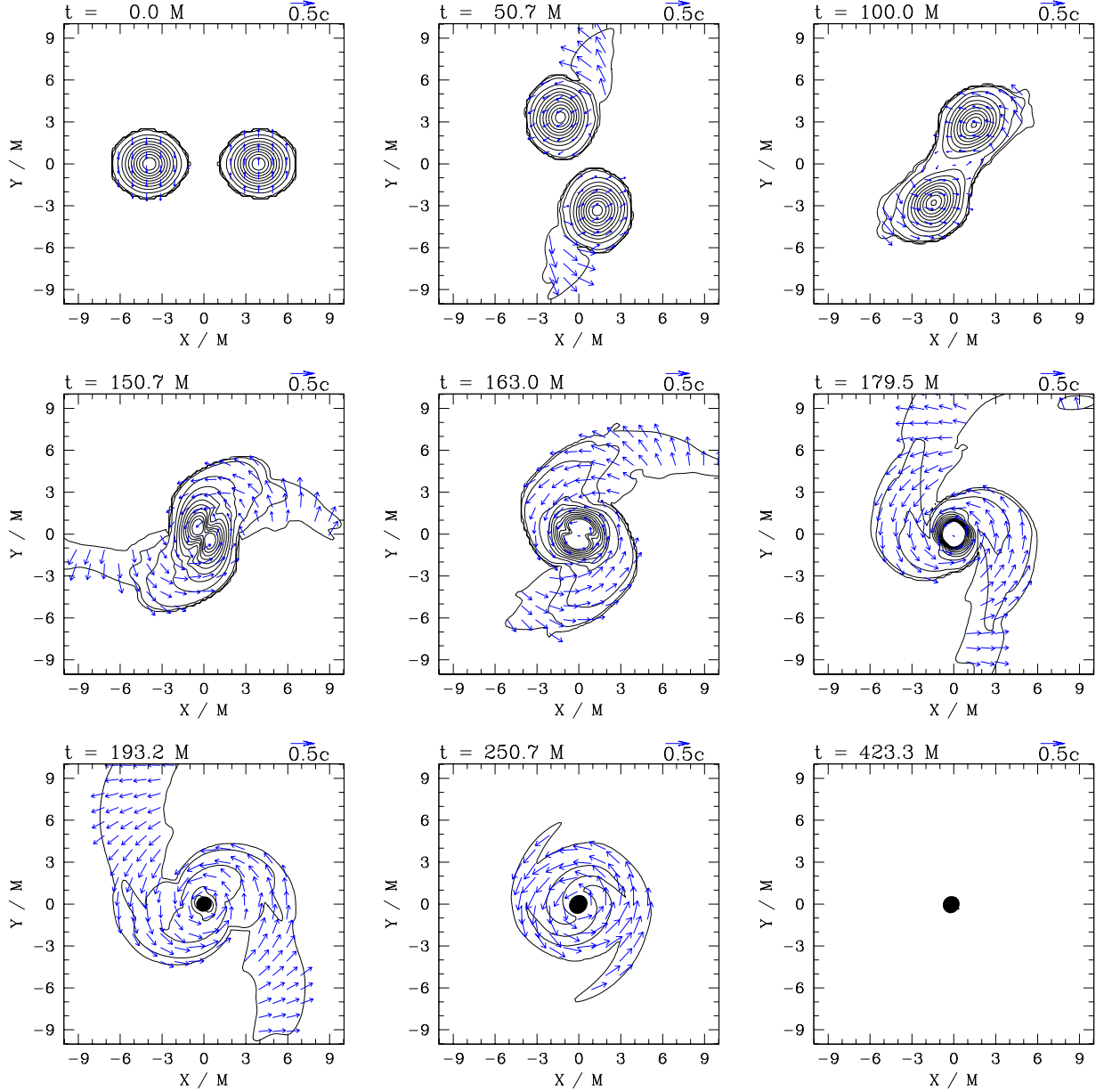


FIG. 12: Same as Fig. 11 but for run M1616B1 (magnetized run).

In summary, we find that the effects of magnetic fields during and shortly after the merger phase are significant but not dramatic. We believe that the most important role of magnetic fields are on the long-term, secular evolution of the merged remnants consisting of a hypermassive neutron star or a black hole surrounded by a disk, as we have demonstrated in our axisymmetric simulations in previous publications [13, 15, 42]. This is not to say that a long-term evolution in 3+1 dimensions is not necessary. For one thing, a 3+1 simulation of the remnants will evolve self-consistently from the NSNS initial data. For the other, MHD turbulence is expected to be more prominent in three dimensions than in axisymmetry [66], and hence may affect the dynamics in

the long-term evolution. We therefore plan to follow the long-term evolution of the remnants in 3+1 dimensions in the future. We thus need to overcome the difficulty of growing constraint violations we observe in our black hole evolutions. We suspect the constraint violations can be controlled by increasing the spatial resolution near the singularity. We currently use a resolution of about $M/7$ near the puncture in our simulations, which is a much lower resolution than the resolutions used in most recent binary black hole simulations. Higher resolution is also required in the case of model M1414 to resolve the MHD instabilities. We also plan to perform simulations of NSNS binaries with larger initial separation. This will allow us to compute the gravitational waveforms with

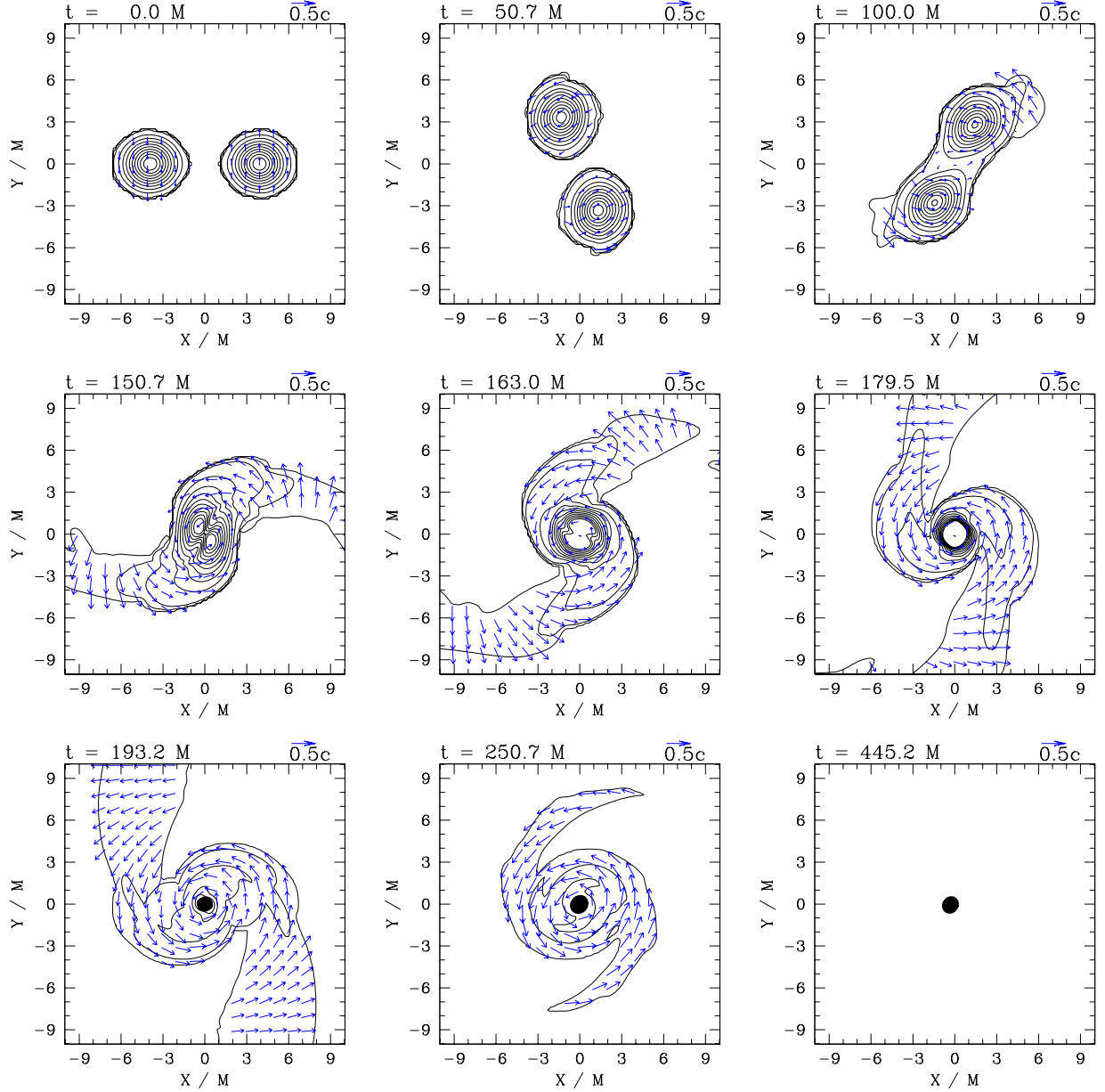


FIG. 13: Same as Fig. 11 but for run M1616B2 (magnetized run).

more cycles so that they can be matched with the post-Newtonian waveforms.

Acknowledgments

Numerical computations were performed on the **abe** cluster at the National Center for Supercomputing Appli-

cations at the University of Illinois at Urbana-Champaign (UIUC). This work was supported in part by NSF Grants PHY02-05155, PHY03-45151, and PHY06-50377 as well as NASA Grants NNG04GK54G and NNX07AG96G at UIUC.

[1] M. Shibata, K. Taniguchi, and K. Uryū, Phys. Rev. D **68**, 084020 (2003), arXiv:gr-qc/0310030.

[2] H. C. Spruit, Astro. & Astrophys. **349**, 189 (1999), arXiv:astro-ph/9907138.

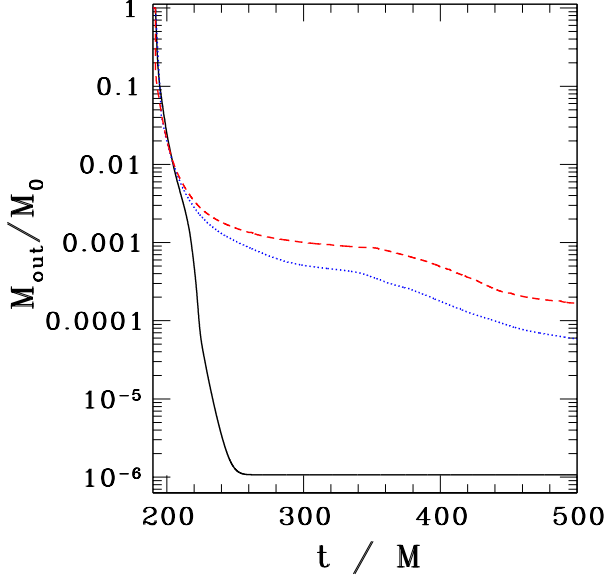


FIG. 14: Rest mass of the material outside the apparent horizon M_{out} for runs M1616B0 (black solid line), M1616B1 (blue dotted line) and M1616B2 (red dash line).

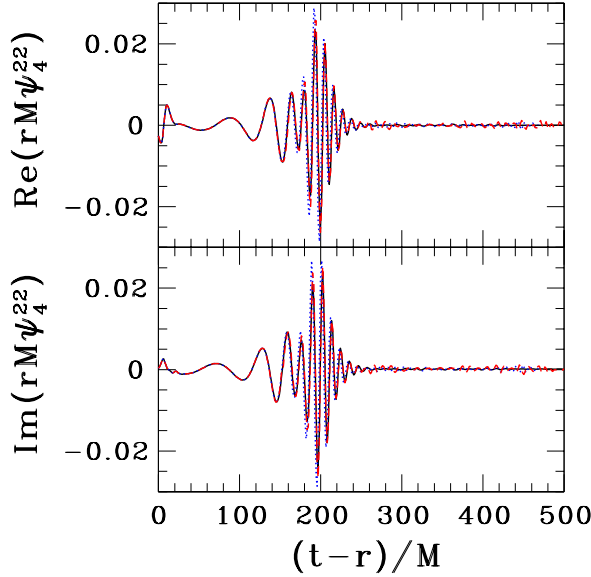


FIG. 15: Gravitation waveform $\psi_4^{22}(t-r)$ for runs M1616B0 (black solid line), M1616B1 (blue dotted line) and M1616B2 (red dash line). Gravitation waves are extracted at radius $r = 43M$.

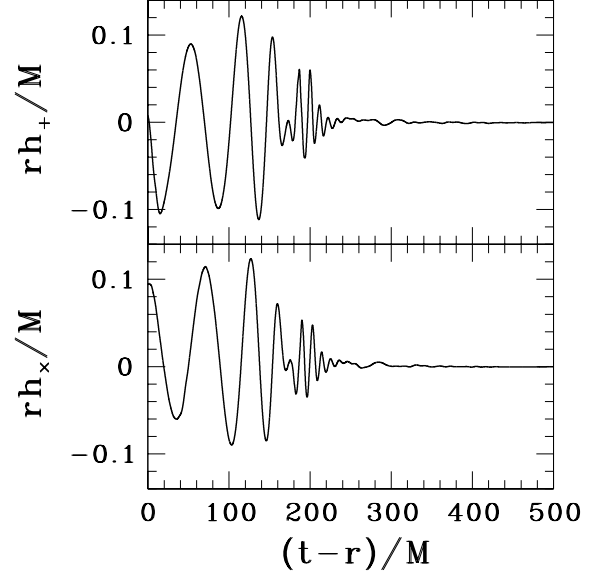


FIG. 16: Gravitation waveform h_+ and h_x for run M1616B0 observed in the direction 45° to the z -axis.

- [3] S. A. Balbus and J. F. Hawley, *Reviews of Modern Physics* **70**, 1 (1998).
- [4] C. Kouveliotou, S. Dieters, T. Strohmayer, J. van Paradijs, G. J. Fishman, C. A. Meegan, K. Hurley, J. Kommers, I. Smith, D. Frail, et al., *Nature (London)* **393**, 235 (1998).
- [5] H. C. Spruit, in *American Institute of Physics Conference Series* (2008), vol. 983 of *American Institute of Physics*

- Conference Series*, pp. 391–398.
- [6] A. I. MacFadyen and S. E. Woosley, *Astrophys. J.* **524**, 262 (1999), arXiv:astro-ph/9810274.
- [7] A. R. King, in *Magnetic Fields in the Universe: From Laboratory and Stars to Primordial Structures.*, edited by E. M. de Gouveia dal Pino, G. Lugones, and A. Lazarian (2005), vol. 784 of *American Institute of Physics Conference Series*, pp. 175–182.
- [8] T. Piran, in *Magnetic Fields in the Universe: From Laboratory and Stars to Primordial Structures.*, edited by E. M. de Gouveia dal Pino, G. Lugones, and A. Lazarian (2005), vol. 784 of *American Institute of Physics Conference Series*, pp. 164–174.
- [9] M. D. Duez, Y. T. Liu, S. L. Shapiro, and B. C. Stephens, *Phys. Rev. D* **72**, 024028 (2005), arXiv:astro-ph/0503420.
- [10] M. Shibata and Y.-I. Sekiguchi, *Phys. Rev. D* **72**, 044014 (2005), arXiv:astro-ph/0507383.
- [11] B. Giacomazzo and L. Rezzolla, *Classical and Quantum Gravity* **24**, 235 (2007), arXiv:gr-qc/0701109.
- [12] M. Anderson, E. W. Hirschmann, S. L. Liebling, and D. Neilsen, *Classical and Quantum Gravity* **23**, 6503 (2006), arXiv:gr-qc/0605102.
- [13] M. D. Duez, Y. T. Liu, S. L. Shapiro, M. Shibata, and B. C. Stephens, *Physical Review Letters* **96**, 031101 (2006), arXiv:astro-ph/0510653.
- [14] M. Shibata, M. D. Duez, Y. T. Liu, S. L. Shapiro, and B. C. Stephens, *Physical Review Letters* **96**, 031102 (2006), arXiv:astro-ph/0511142.
- [15] M. D. Duez, Y. T. Liu, S. L. Shapiro, M. Shibata, and B. C. Stephens, *Phys. Rev. D* **73**, 104015 (2006), arXiv:astro-ph/0605331.
- [16] M. Shibata, Y. T. Liu, S. L. Shapiro, and B. C. Stephens, *Phys. Rev. D* **74**, 104026 (2006), arXiv:astro-ph/0610840.
- [17] M. Shibata and K. Uryū, *Phys. Rev. D* **74**, 121503(R) (2006).

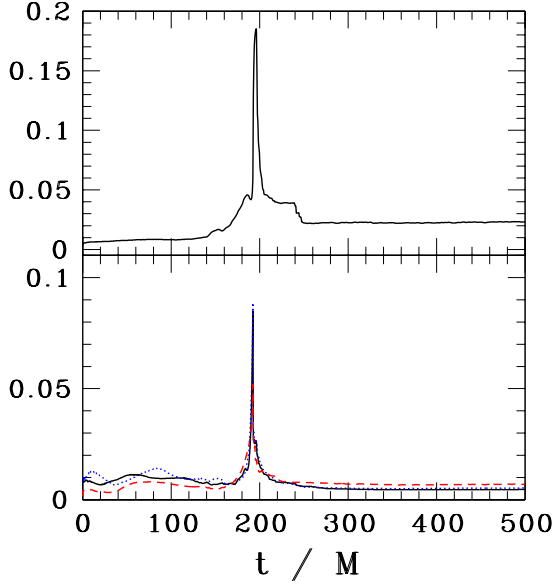


FIG. 17: Constraint violations for the unmagnetized run M1414B0. Upper panel: Normalized L2 norm of the Hamiltonian constraint. Lower panel: Normalized L2 norm of the x (black solid line), y (blue dotted line) and z (red dash line) components of the momentum constraint. Note that the large violations corresponding to the peaks at $t = 192M$ are trapped inside the event horizon. When the apparent horizon is detected ($t > 192M$), the constraints are computed only in the region outside the horizon.

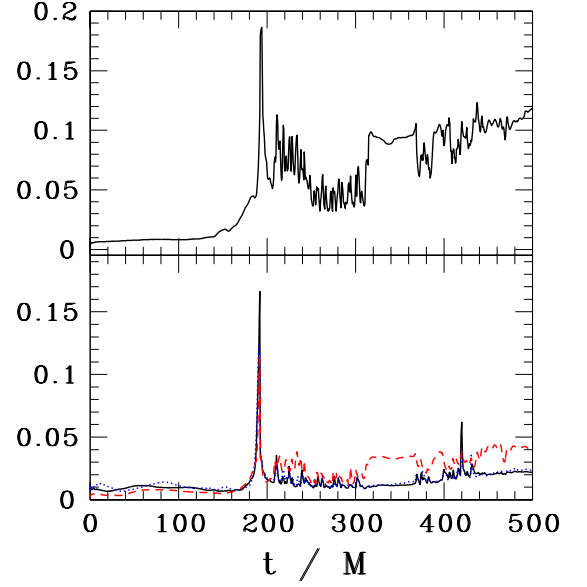


FIG. 18: Same as Fig. 17 but for the magnetized run M1414B1.

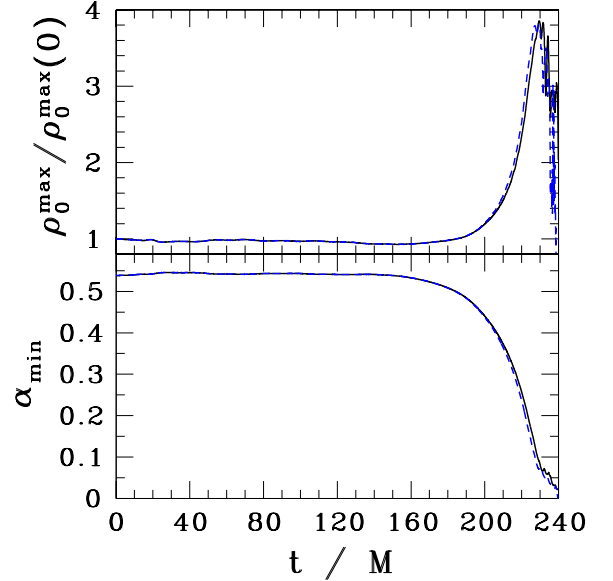


FIG. 19: Evolution of maximum density ρ_0^{\max} and minimum lapse α_{\min} for unmagnetized (black solid line) and magnetized (blue dash line) runs of model M1418. The merger occurs at $t \approx 180M$, and an apparent horizon appears at $t = 232M$ for both magnetized and unmagnetized cases.

- [18] M. Shibata and K. Uryū, *Class. Quant. Grav.* **24**, 125 (2007).
- [19] M. Shibata and K. Taniguchi, *ArXiv e-prints* **711** (2007), 0711.1410.
- [20] Z.B. Etienne, J.A. Faber, Y.T. Liu, S.L. Shapiro, K. Taniguchi, and T.W. Baumgarte, *Phys. Rev. D*, in press (arXiv:0712.2460).
- [21] Y. T. Liu, S. L. Shapiro, and B. C. Stephens, *Phys. Rev. D* **76**, 084017 (2007), arXiv:0706.2360.
- [22] Z. B. Etienne, J. A. Faber, Y. T. Liu, S. L. Shapiro, and T. W. Baumgarte, *Phys. Rev. D* **76**, 101503 (2007), arXiv:0707.2083.
- [23] M. Shibata and K. ō. Uryū, *Phys. Rev. D* **61**, 064001 (2000), arXiv:gr-qc/9911058.
- [24] M. Shibata and K. Uryū, *Progress of Theoretical Physics* **107**, 265 (2002), arXiv:gr-qc/0203037.
- [25] M. Shibata, K. Taniguchi, and K. Uryū, *Phys. Rev. D* **71**, 084021 (2005), arXiv:gr-qc/0503119.
- [26] M. Shibata and K. Taniguchi, *Phys. Rev. D* **73**, 064027 (2006), arXiv:astro-ph/0603145.
- [27] M. Anderson, E. W. Hirschmann, L. Lehner, S. L. Liebling, P. M. Motl, D. Neilsen, C. Palenzuela, and J. E. Tohline, *Phys. Rev. D* **77**, 024006 (2008), arXiv:0708.2720.
- [28] M. Anderson, E. W. Hirschmann, L. Lehner, S. L. Liebling, P. M. Motl, D. Neilsen, C. Palenzuela, and J. E. Tohline, *ArXiv e-prints* **801** (2008), 0801.4387.
- [29] Note that it is the total rest mass that is conserved during the evolution. The rest mass of each NS in the binary is obtained by solving the Tolman-Oppenheimer-Volkov

- (TOV) equations with the same EOS and central density as those in [27].
- [30] E. Berti, S. Iyer, and C. M. Will, *ArXiv e-prints* **709** (2007), 0709.2589.
- [31] G. B. Cook, S. L. Shapiro, and S. A. Teukolsky, *Astrophys. J.* **422**, 227 (1994).
- [32] J. G. Baker, J. Centrella, D.-I. Choi, M. Koppitz, and J. van Meter, *Phys. Rev. Lett.* **96**, 111102 (2006).

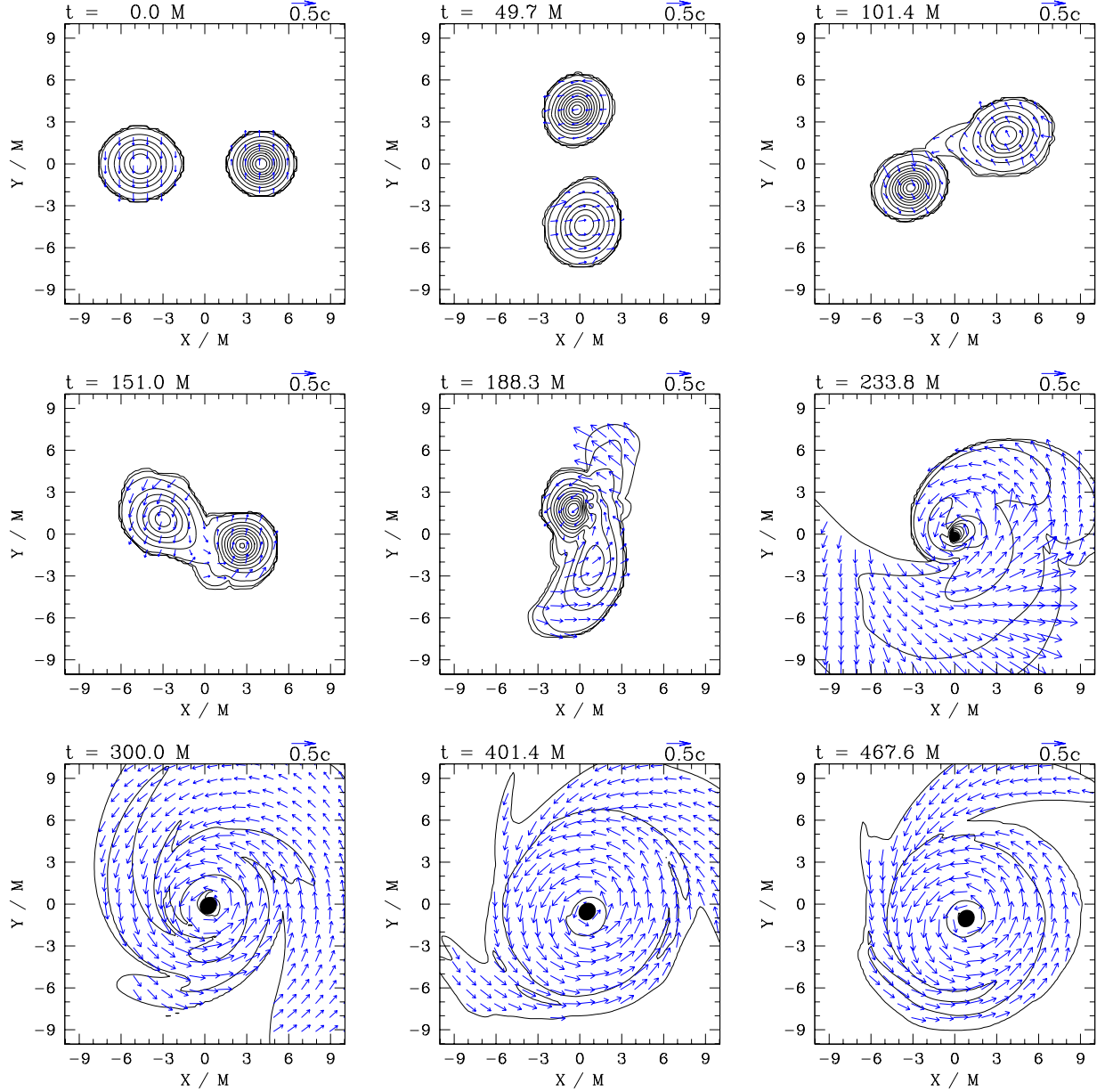


FIG. 20: Same as Fig. 11 but for run M1418B0 (unmagnetized run).

- [33] M. Campanelli, C. O. Lousto, P. Marronetti, and Y. Zlochower, *Phys. Rev. Lett.* **96**, 111101 (2006).
- [34] R. C. Duncan and C. Thompson, *Astro. J. Lett.* **392**, L9 (1992).
- [35] J. C. McKinney and C. F. Gammie, *Astrophys. J.* **611**, 977 (2004), arXiv:astro-ph/0404512.
- [36] J.-P. De Villiers, J. F. Hawley, and J. H. Krolik, *Astrophys. J.* **599**, 1238 (2003), arXiv:astro-ph/0307260.
- [37] J.-P. De Villiers, J. F. Hawley, J. H. Krolik, and S. Hirose, *Astrophys. J.* **620**, 878 (2005), arXiv:astro-ph/0407092.
- [38] J.-P. De Villiers, J. Staff, and R. Ouyed, *ArXiv Astrophysics e-prints* (2005), astro-ph/0502225.
- [39] J. C. McKinney, *Mon. Not. R. Astro. Soc.* **368**, 1561 (2006), arXiv:astro-ph/0603045.
- [40] Y. Mizuno, K.-I. Nishikawa, S. Koide, P. Hardee, and G. J. Fishman, *ArXiv Astrophysics e-prints* (2006), astro-ph/0609344.
- [41] S. Koide, K. Shibata, T. Kudoh, and D. L. Meier, *Science* **295**, 1688 (2002).
- [42] B. C. Stephens, S. L. Shapiro, and Y. T. Liu, *Phys. Rev. D* **77**, 044001 (2008), arXiv:0802.0200.
- [43] T. W. Baumgarte and S. L. Shapiro, *Phys. Rev. D* **59**, 024007 (1998).
- [44] M. Shibata and T. Nakamura, *Phys. Rev. D* **52**, 5428 (1995).
- [45] J. R. van Meter, J. G. Baker, M. Koppitz, and D.-I. Choi, *Phys. Rev. D* **73**, 124011 (2006).
- [46] <http://www.cactuscode.org/>.
- [47] J. Thornburg, *Class. Quant. Grav.* **21**, 743 (2004).
- [48] M. D. Duez, P. Marronetti, S. L. Shapiro, and T. W.

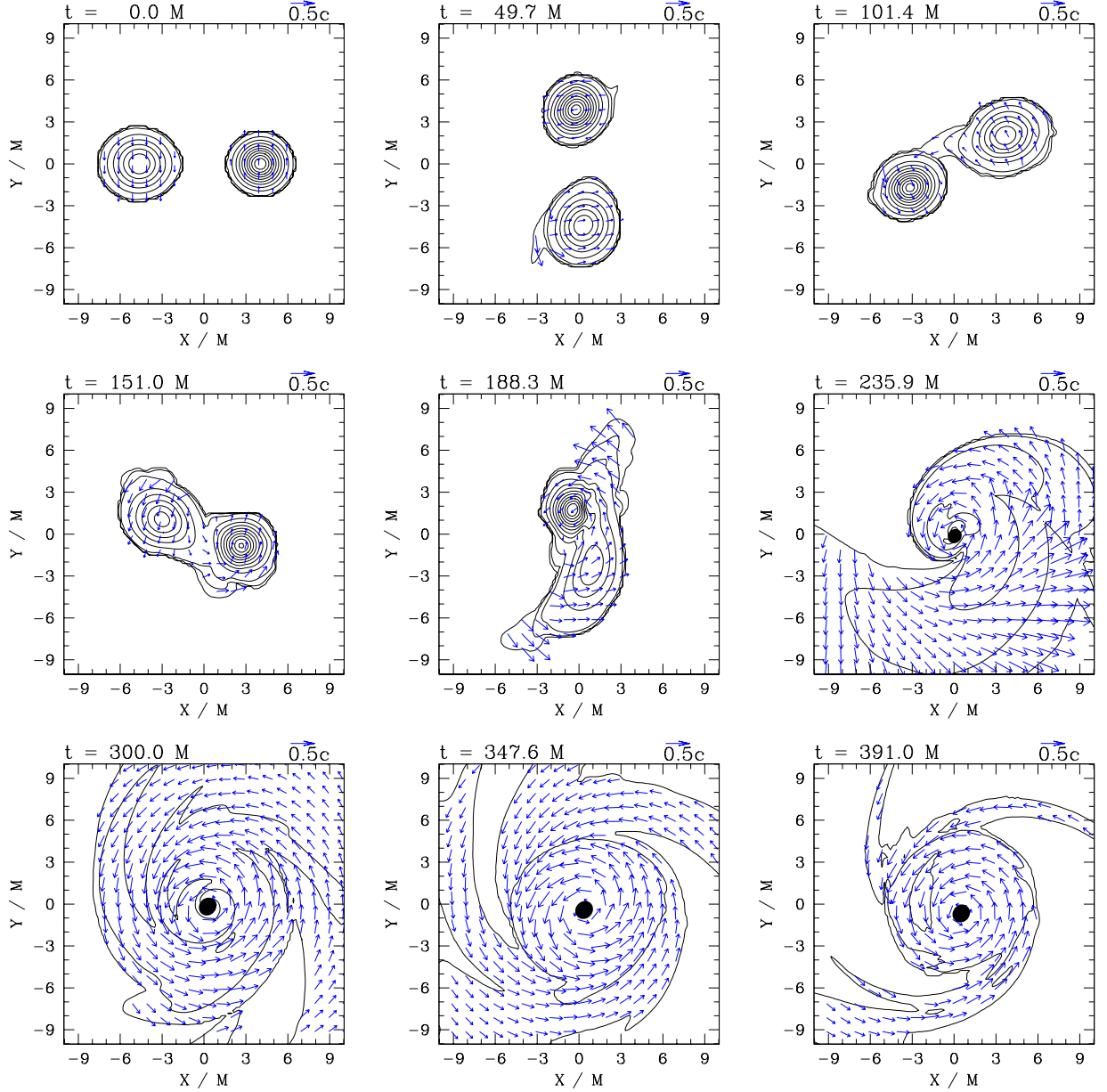


FIG. 21: Same as Fig. 11 but for run M1418B1 (magnetized run).

- Baumgarte, Phys. Rev. D **67**, 024004 (2003), arXiv:gr-qc/0209102.
- [49] B. van Leer, Journal of Computational Physics **23**, 276 (1977).
- [50] A. Harten, P. Lax, and B. van Leer, SIAM Rev. **25**, 35 (1983).
- [51] G. Tóth, Journal of Computational Physics **161**, 605 (2000).
- [52] C. F. Gammie, J. C. McKinney, and G. Tóth, Astrophys. J. **589**, 444 (2003), arXiv:astro-ph/0301509.
- [53] Z. B. Etienne, J. A. Faber, Y. T. Liu, S. L. Shapiro, and T. W. Baumgarte, Phys. Rev. D **76**, 101503 (2007), arXiv:0707.2083.
- [54] J. A. Faber, T. W. Baumgarte, Z. B. Etienne, S. L. Shapiro, and K. Taniguchi, Phys. Rev. D **76**, 104021 (2007), arXiv:0708.2436.
- [55] B.D. Farris, T.K. Li, Y.T. Liu, and S.L. Shapiro, submitted to Phys. Rev. D (arXiv:0802.3210).
- [56] K. Taniguchi and E.ourgoulhon, Phys. Rev. D **66**, 104019 (2002), arXiv:gr-qc/0207098.
- [57] K. Taniguchi and E.ourgoulhon, Phys. Rev. D **68**, 124025 (2003), arXiv:gr-qc/0309045.
- [58] G. B. Cook, S. L. Shapiro, and S. A. Teukolsky, Astrophys. J. **398**, 203 (1992).
- [59] J. A. Font, T. Goodale, S. Iyer, M. Miller, L. Rezzolla, E. Seidel, N. Stergioulas, W.-M. Suen, and M. Tobias, Phys. Rev. D **65**, 084024 (2002), arXiv:gr-qc/0110047.
- [60] K. Ioka and K. Taniguchi, Astrophys. J. **537**, 327 (2000), arXiv:astro-ph/0001218.
- [61] M. Vasúth, Z. Keresztes, A. Mihály, and L. Á. Gergely,

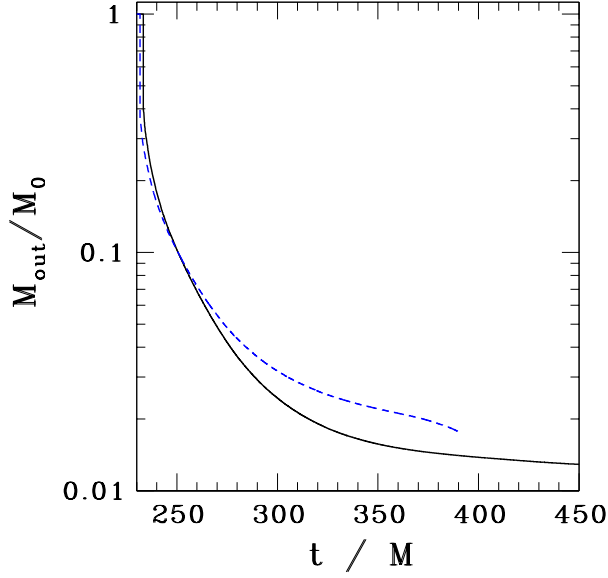


FIG. 22: Rest mass of the material outside the apparent horizon M_{out} for the unmagnetized (black solid line) and magnetized (blue dash line) runs of model M1418.

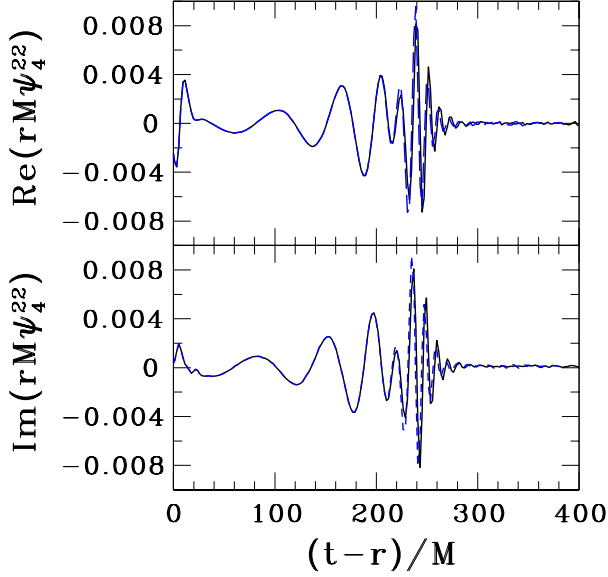


FIG. 23: Gravitation waveform $\psi_4^{22}(t-r)$ for unmagnetized (black solid line) and magnetized (blue solid line) runs of model M1418. Gravitation waves are extracted at radius $r = 43M$.

- Phys. Rev. D **68**, 124006 (2003), arXiv:gr-qc/0308051.
- [62] B. Mikóczy, M. Vasúth, and L. Á. Gergely, Phys. Rev. D **71**, 124043 (2005), arXiv:astro-ph/0504538.
- [63] M. Alcubierre, B. Brügmann, P. Diener, M. Koppitz, D. Pollney, E. Seidel, and R. Takahashi, Phys. Rev. D **67**, 084023 (2003), arXiv:gr-qc/0206072.
- [64] M. Campanelli, C. O. Lousto, and Y. Zlochower, Phys. Rev. D **73**, 061501 (2006).
- [65] T. Piran, Reviews of Modern Physics **76**, 1143 (2005), arXiv:astro-ph/0405503.
- [66] J. F. Hawley, Astrophys. J. **528**, 462 (2000), arXiv:astro-ph/9907385.